SCANNING LASER ACOUSTIC MICROSCOPE VISUALIZATION OF SOLID INCLUSIONS IN SILICON NITRIDE

D. E. Yuhas, T. E. McGraw and L. W. Kessler
Sonoscan, Inc.
Bensenville, Illinois 60106

ABSTRACT

The Scanning Laser Acoustic Microscope (SLAM) operating at a frequency of 100 MHz is used to characterize solid inclusions in silicon nitride. Ten, seven millimeter thick discs, with 100 and 400 micron implanted inclusions are analyzed. We find that the images of a solid inclusion are characterized by a bright high transmission central zone, a well defined dark boundary and a characteristic diffraction ring pattern. These image features differentiate solid inclusions from pores and voids which may also be encountered in the samples. The images of the implanted flaws were generally found to be larger than anticipated. This can be understood in terms of the divergence of the sound due to diffraction and due to lens action of the curved boundary of the flaw. Our initial observations suggest that accurate estimates of defect size may be obtainable from a more complete analysis of SLAM micrographs.

INTRODUCTION

The acoustic signatures of a variety of flaw types, e.g. cracks, delaminations, solid inclusions, etc. were presented in a companion paper[1]. This paper concentrates on characterizing solid inclusions, specifically, silicon, carbon and iron inclusions within hot pressed silicon nitride.

The approach adopted is empirical. Image features of flaws found in these discs are compared with those found in other samples where the flaw type was confirmed by destructive analysis. The image features derived in this manner were subsequently found to compare well with those predicted based on elementary scattering theory[2].

THE TECHNIQUE AND SAMPLES

All samples were analyzed using a commercially available scanning laser acoustic microscope operating at a frequency of 100 MHz. Introductory material describing acoustic micrographs and the SLAM are presented elsewhere[1].

A total of 10 samples were investigated using the Scanning Laser Acoustic Microscope. Each sample was in the form of a disc approximately 25 mm in diameter and ranging from 6 to 7 mm thick. The sample identification, the bulk density and size and type of implanted inclusion are listed in Table I. Although the intended size and type of each inclusion was known prior to the investigation, its actual size and location were not. This led to some confusion since in many samples, several inclusions were found; not all of them were intended. Furthermore, several samples contained inhomogeneous porosity distributions which may have been inadvertently introduced in the "seeding" process.

TABLE I

Sample ID #	Density gm/cm^3	Presumed Flaw Type	Presumed Flaw Type (Diameter-Microns)
65	3.01	Iron	100
88	3.03	Iron	400
29	3.21	Iron	400
90	-	Iron	400
32	2.94	Silicon	100
51	2.94	Silicon	400
49	-	Silicon	400
45	3.10	Carbon	100
5	3.04	Carbon	400
73	3.21	Carbon	400

NOTE: Fully dense Si_3N_4 has a density of $3.21\ g/cm^3$.

MATERIAL CHARACTERIZATION

From Table I, we see that the density of the sample discs varies over 9 percent range from a high density of $3.21\ gm/cm^3$ to a low of $2.94\ gm/cm^3$. The density of the sample correlated with the observed ultrasonic attenuation and the structural features in the micrographs. Figure 1 shows three acoustic micrographs obtained on samples with measured densities of 3.21, 3.10, and $2.94\ gm/cm^3$ respectively. The variation in the micrograph characteristics with density is quite dramatic and can be readily recognized. Most samples were investigated "as supplied" with a fairly coarse surface grind finish. Although the grind marks are visible in the micrographs, they did not preclude location and identification of the buried flaws. Some of the samples reported here using the SLAM were subsequently examined by Kino, et al at Stanford University with a higher

frequency pulse echo system[3]. For this examination, however, the samples had to be surface lapped and polished in order to make them compatible. After the pulse echo work, one of the samples (#73) was again returned to Sonoscan for a repeat SLAM investigation. The surface polish made the SLAM micrographs prettier but it did not alter the findings.

Figure 1a is an amplitude micrograph of Sample 73 illustrating the typical acoustic microstructure encountered in the high density samples (ρ = 3.21 gm/cm^3). The intensity across this 2 mm field of view is "relatively" uniform exhibiting only low contrast features. The vertical linear structures are the result of the surface texture.

Figure 1b is an amplitude micrograph of Sample 45 (ρ = 3.10 gm/cm^3), illustrating the typical acoustic microstructure. Notice the non-uniformity in acoustic transmission observed in this 3 mm field of view. Some of the larger regions of decreased transmission are noted with arrows. The regions of low transmission are attributable to energy losses at embedded clusters of pores. The non-uniform distribution of porosity of this sample, relative to the high density samples, lends the acoustic image a characteristic visual texture. Note the surface texture is also evident in this micrograph (vertical, linear structures).

Figure 1c is an amplitude micrograph of Sample 51, ρ = 2.94 gm/cm^3, the typical acoustic microstructure encountered in the low density samples is illustrated in this 3 mm field of view. The substantial transmission variation is attributed to the non-uniform distribution of porosity (relative to Sample 73). Relative to Sample 45, the porosity is segregated in larger zones. Attenuating zones, indicative of increased porosity are typically 1.0 to 2.5 millimeters (largest dimension).

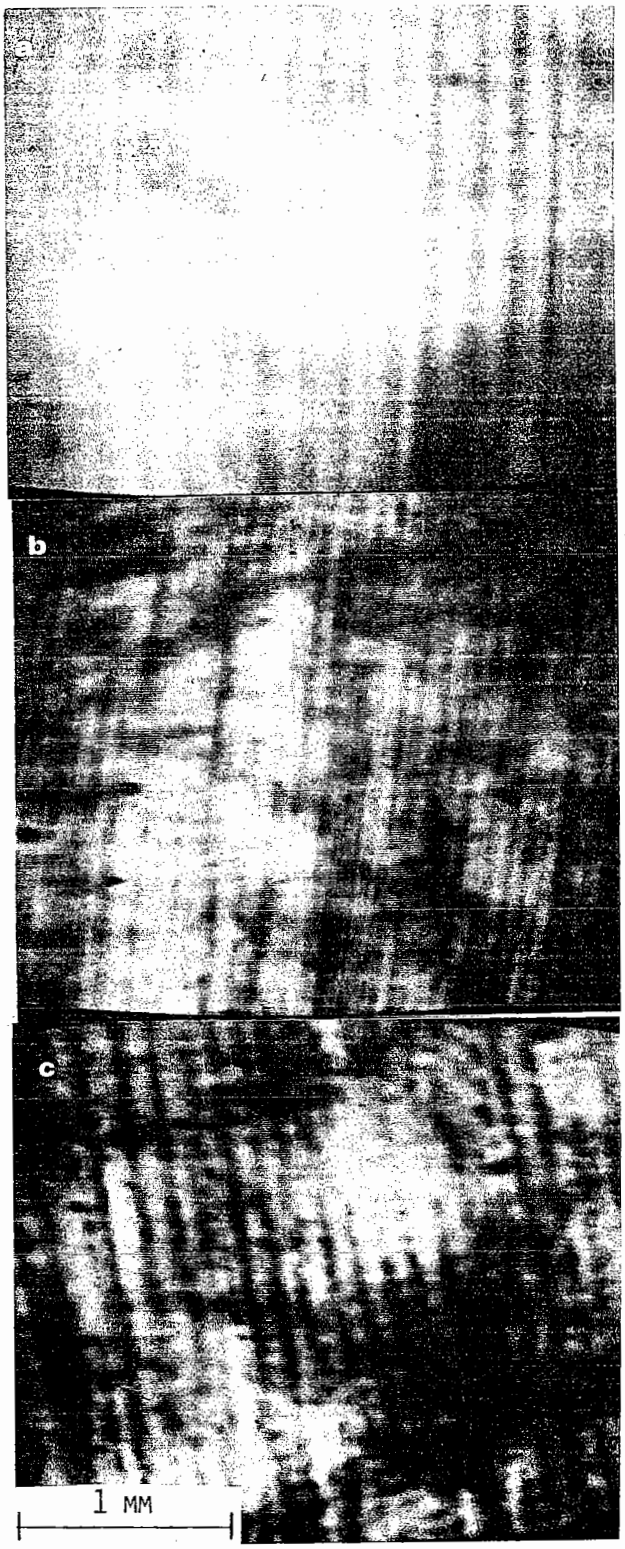

Fig. 1 - SLAM micrographs showing typical silicon nitride for a range of bulk densities.

a) = 3.21 gm/cm^3
b) = 3.10 gm/cm^3
c) = 2.94 gm/cm^3

The particularly peculiar porosity distribution found in Sample 51 is illustrated in Figure 2. Both the amplitude micrograph (a) and the interferogram (b) are presented. Three, large (1 mm) highly attenuating zones are apparent in this field of view. A large number of these flaws was found in a rectangular zone 6 mm by 12 mm in size.

Depth determination of the three flaws in Figure 1 indicate that they are located in a single plane near the center of the sample (3.3 mm below the surface). Although the presence of the attenuating zones leads to a complex background structure, they are morphologically distinct from solid inclusions and can be differentiated easily.

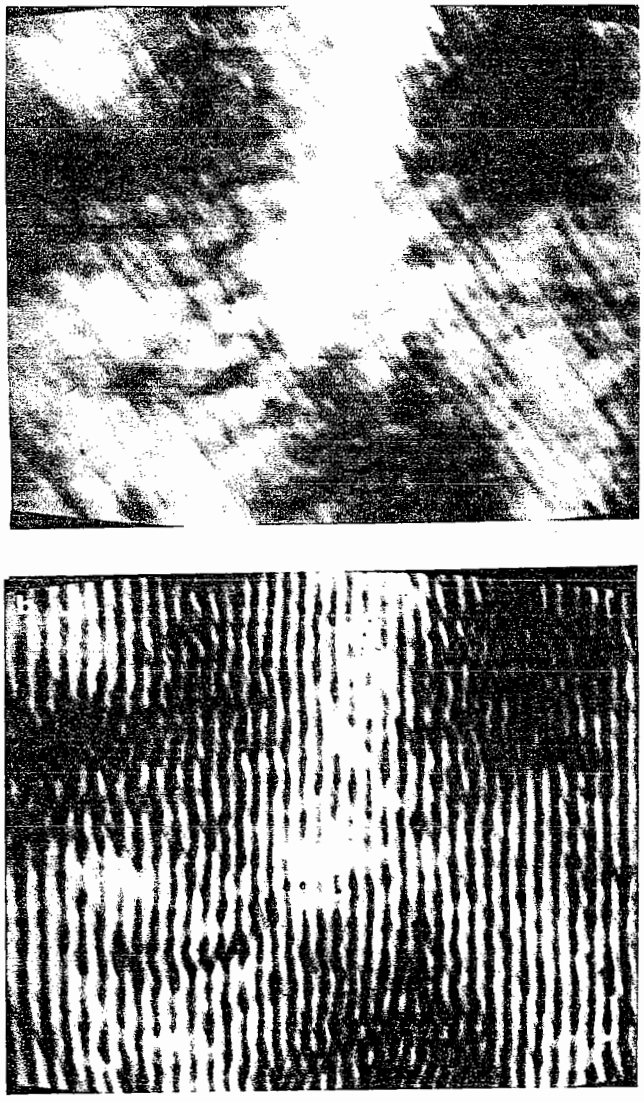

Fig. 2 - Three zones of high attenuation attributed to increased porosity.

a) amplitude micrograph
b) interferogram.

Field of view is 3.0 by 2.3 millimeters.

SOLID INCLUSIONS

Table II summarizes the results obtained on the 10 samples analyzed. The Table lists only those flaws which can be interpreted of solid inclusions. The recognition criteria are: 1). a central zone whose acoustic transmission is brighter than or comparable to that in the host Si_3N_4. 2). a well-defined boundary, 3). a ring pattern associated with the diffraction of sound by the inclusion. Other flaw types with features similar to those depicted in Figures 1 and 2 were attributed to porosity and were not singled out for further analysis. At least one solid inclusion was detected in each sample and in several cases multiple flaws were encountered. Two of the samples were systematically scanned (#51 and #73) and all detected solid inclusions photodocumented. In the other samples, only the most apparent flaws were analyzed and presented in the Table.

Before discussing the various flaw types and presentation of SLAM micrographs, a few points should be made concerning the data in Table II. Flaw image size as given in the Table is measured directly from the acoustic micrographs. In the cases where the flaws are circular, the diameter, measured from the middle of the first diffraction ring, is given. For elliptical flaws, the major and minor axis are given. For irregularly shaped flaws, the maximum and minimum dimensions of the flaws are given. It must be kept in mind that the SLAM images are orthographic projection images.

TABLE II

Sample Number	Defect Identification	Image Size (Microns)	Depth (mm)	Shear Wave Image	Compressional Wave Image	Comment	Intended Flaw
5	a	640	4.7	Best	Yes	Circular, medium contrast	400 micron carbon
5	b	200	-	No	Yes	Circular, low contrast	
73	a	690	4.9	Best	Yes	Circular, high contrast	400 micron carbon
73	a	490	2.1	Best	Yes	Same flaw from other side	
45	a	150	-	Best	No	Circular, low contrast, near edge	100 micron carbon
90	a	625	-	Yes	Yes	High contrast elliptical	400 micron Iron
29	a	530x370	3.5	Best	Yes	Irregular shape, med. contrast	
29	b	165x350	-	No	Yes	Irregular, med. contrast	400 micron Iron
88	a	550	3.6	Best	Yes	Circular Low contrast	
88	b	100	Near Surface	No	Yes	Circular Low contrast	400 micron Iron
65	a	280x190	-	Yes	No	Irregular, difficult to distinguish from porosity	100 micron Iron
51	a	175	0.9	Yes	Yes	Very high contrast circular	400 micron silicon
51	a	750	6.0	Yes	Yes	Same flaw from other side	
51	b	Two Flaws 60	Near Surface	Yes	Yes	Two close lying 60 micron flaws	
51	c	225	Near Surface	No	Yes	Bright, circular, low contrast	
51	d	250	-	Yes	No	Low contrast, circular	
51	e	450	-	No	Yes	Triangular, Low contrast	
49	a	780	-	No	Yes	Very low contrast circular	400 micron silicon
32	a	225	-	Yes	No	Circular, very low contrast	100 micron silicon

Thus, the recorded image size may differ from the actual flaw size and will also depend on depth below the observation plane. In general, we expect the soundfield to diverge from the flaw site which leads to image sizes typically larger than the actual flaw size. This would be true for any imaging technique.

Column 4 lists depth determinations. This is determined by stereoscopy which is illustrated in Figure 3. Stereoscopy involves imaging the same flaw at two different angles of insonification. By measuring the shift in the projected image position of the flaw (relative to a fixed point on surface) the flaw depth can be determined. Because the depth determination by stereoscopy uses the acoustic images, the accuracy is governed by image resolution (30 microns for shear waves).

The fifth and sixth columns refer to flaw "visibility" for different methods of examination. Two methods were employed. For shearwave investigations a plane wave is incident on the sample at an angle of $9,4^{\circ}$ from the normal through a water couplant. This is beyond the compressional wave critical angle; only shearwaves propagate and are responsible for the image. For compressional wave investigations, an acoustic plane wave is normally incident, only compressional waves are incident upon the flaw. Experimentally, we have found definite preferences for shear or compressional insonification to optimize visibility of defect. Three levels of flaw visibility are listed: "yes"- detectable; "no" - non-detectable and "best" - optimum flaw visualization. For those flaws where visibility was similar for both methods, both columns are marked "yes".

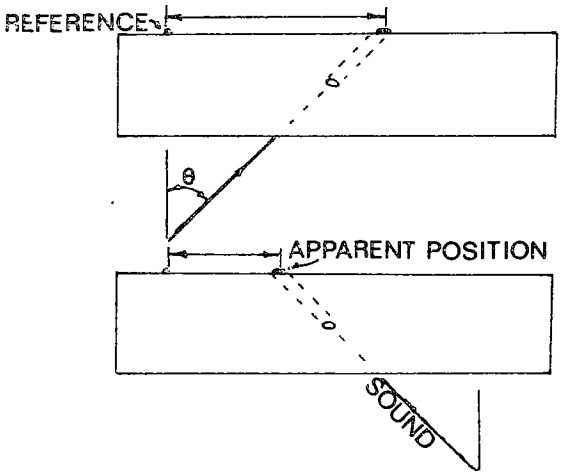

Fig. 3 - Schematic illustrating depth determination by stereoscopy.

Carbon Inclusions - Three samples were investigated which contained implanted carbon inclusions, #5, #73, and #45). In each case the images (Flaws 5a, 73a and 45a) were circular. Visibility was optimum with shear wave insonification, however, each of the 400 μ flaws were detectable with either compressional or shear waves. On the other hand, the 100 micron carbon flaw was only detected with shear waves. Of this group, the flaw implanted in Sample 73 exhibits the highest contrast and is most easily detected. Acoustic micrograph of this flaw is given in Figure 4a. The smaller flaw found in Sample #45 is presented in Figure 4b.

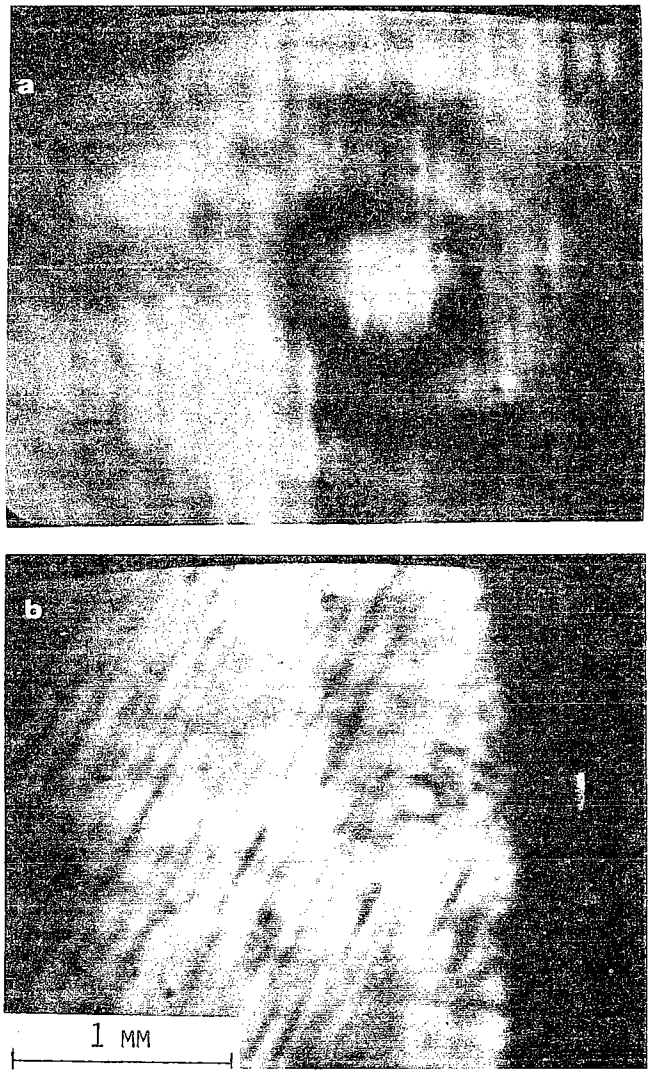

Fig. 4 - SLAM images of implanted carbon inclusion in silicon nitride discs.

a) Sample 73

b) Sample 45

In order to accurately estimate flaw dimensions from acoustic images, proper account must be taken of beam spreading and possible focusing. To illustrate the magnitude of the effects, a single flaw was imaged at two different depths in a sample. Sample 73 was convenient since the flaw is located 2.1 mm below one surface and 4.9 mm below the other. The difference in image size was found to be 490 microns compared with 690 microns as the flaw is observed from opposite surfaces. After destructive analysis of this sample to reveal the actual flaw size, an accurate formula can be obtained for flaw size determination from the image dimensions and depth.

Iron Inclusions - Four samples analyzed contained implanted iron inclusions, 3 contained 400 micron flaws, the other contained a100 micron flaw. The detected flaws showed considerable variation in both degree of contrast and morphology. For example, the flaw detected in Sample #90 shows a symmetric circular pattern surrounded by several well-developed diffraction rings. The flaw found in #88 (flaw 88a) is also circular but exhibits lower contrast and was more difficult to detect. In Sample #29 (400 u Fe) the contrast is similar to that of Sample #90, however, the shape is quite irregular and a well-developed diffraction ring pattern was not observed. Similarly, the smaller flaw detected in Sample #65 (100 u, Fe) has an irregular shape. Flaw found in Sample #90 is compared with that of #29 in Figure 5.

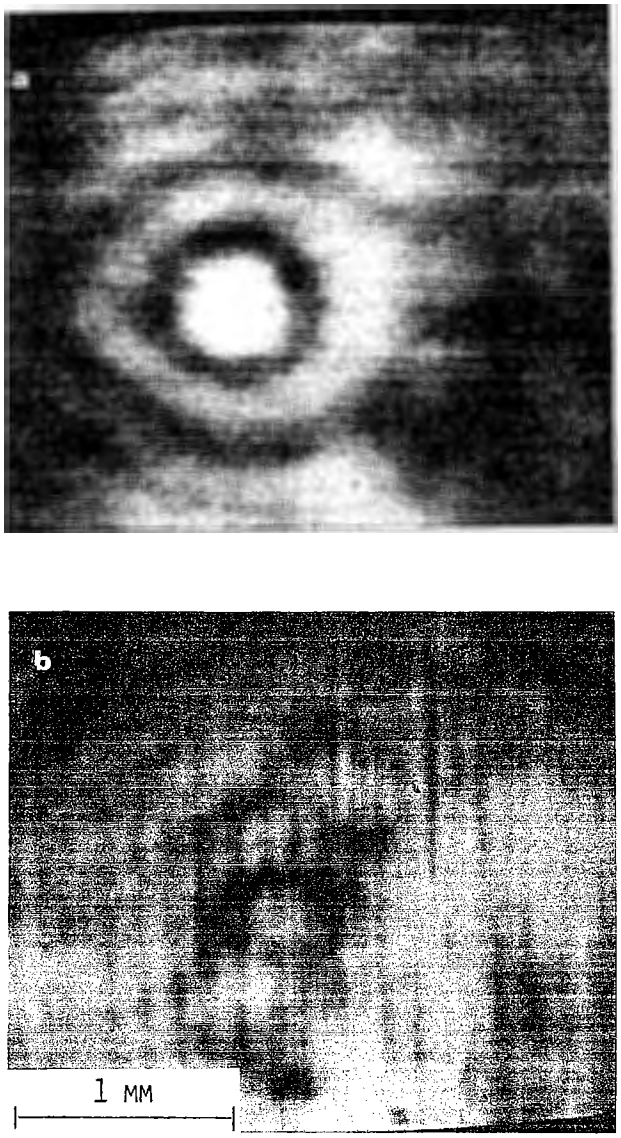

Fig. 5 - SLAM micrograph of implanted Iron inclusions in Samples 90 and 29 respectively.

Silicon Inclusions - Three samples were analyzed which had implanted silicon inclusions. A complete analysis was carried out on Sample #51 where five flaws, with features characteristic of solid inclusions, were found. This sample was a low density sample (ρ = 2.94 gm/cm^2) and substantial acoustic transmission variations (attributed to increased porosity) were found. Four of the flaws were relatively low contrast features and one exhibited high contrast with a well developed diffraction ring pattern. Visibility of this high contrast flaw was similar using shear and compressional waves. The image of this high contrast flaw is shown in Figure 6. Both a compressional (6a) and shear wave (6b) images are presented for comparison.

For silicon inclusions, the visibility is comparable for both insonification modes. The elliptical characteristic of the flaw in Figure 6b is attributable to the angular insonification. A sphere will project an elliptical image using angle beam shear wave insonification. Another point to be made with regards to this flaw is the large increase in image size with flaw depth. In Figure 6, the flaw lies 0.9 mm below the observation plane. This flaw is also detectable at the opposite surface of the disc where it is 6 mm below the observation plane. The image sizes are 175 and 750 microns respectively.

Flaws found in samples number 49 and 32 exhibit some anomalous behavior. Although circular, like flaw image 51a, they show much less contrast. Additionally, the large circular flaw in #49 was detectable only with compressional insonification while the flaw in Sample #32 was found only with shear waves.

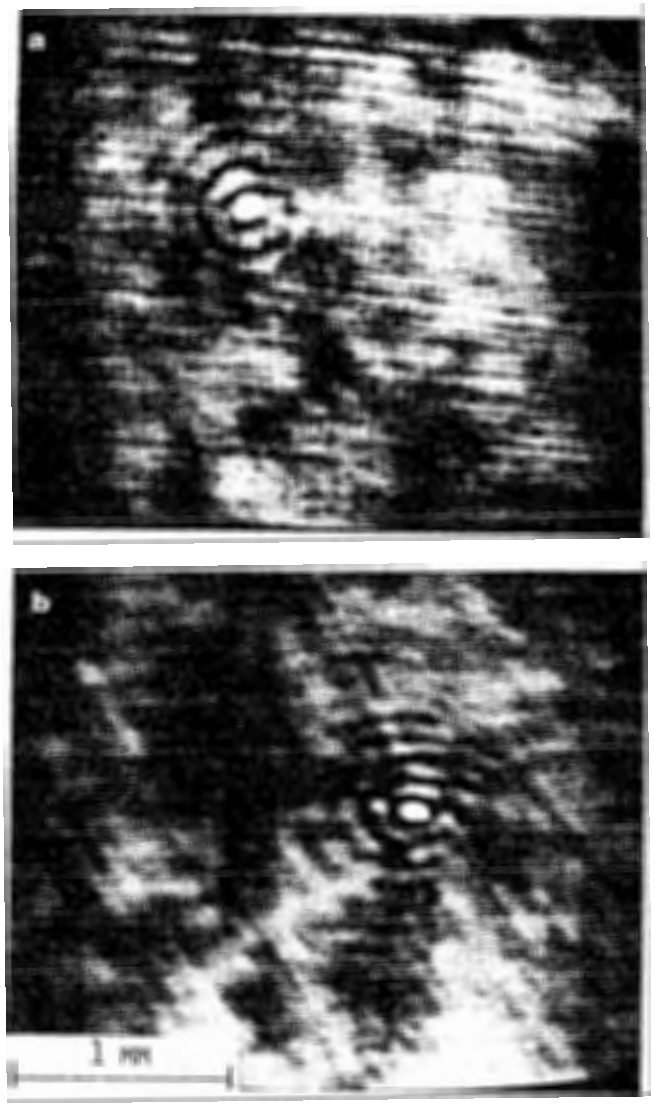

Fig. 6 - Comparison of compressional (a) and shear wave (b) images of inclusion 51a.

SUMMARY

This investigation represents only the initial step in delineating the characteristics of solid inclusions in hot-pressed silicon nitride. The imaging capability is found to be essential for the recognition and differentiation of flaws. The unique characteristics of these implanted inclusions were found to be: 1) the presence of high acoustic transmission centers, 2) well defined boundaries and, 3) diffraction ring patterns. These features serve to distinguish solid inclusion from laminar flaws, cracks and porosity variations. Solid inclusion characteristics observed in this study have subsequently been shown to have obvious similarities with those predicted by elementary scattering theory[2]. Although qualitative agreement exists between theory and experiment, direct analysis, the same flaw analyzed experimentally, theoretically and destructively, has yet to be done.

Defect size estimates can be made by measuring the image sizes recorded on the acoustic micrographs. However, it is clear that such determinations need to be corrected for defect depth. Additionally, qualitative observations of variations in defect contrast as well as shape may prove to be useful in identifying specific types of solid inclusions. Unfortunately, definitive conclusions cannot be made because of a great uncertainty in the actual size and type of inclusions in the samples investigated. Our observations demonstrating a multiplicity of flaws when only one was intended, coupled with the discovery of complex chemical reactions between the implanted inclusions and the host silicon nitride[8] make interpretation of some of our observations to be somewhat speculative. Validation of flaw dimensions and type by destructive analysis needs to be done.

We anticipate that a detailed image analysis using either scattering theory or direct holographic reconstruction will take full advantage of all the information available in SLAM micrographs. This approach coupled with adequate destructive analysis will lead to accurate defect sizing and differentiation of the various solid inclusion types. Furthermore, in other studies involving the SLAM, we have shown that results obtained on samples with simple shapes are similar to those found on complex production components[4-7]. The SLAM is the only high frequency ultrasonic technique which has demonstrated the capability to deal with complex shapes. In these studies, where the primary interests involved detection of cracks and porosity routine non-destructive testing procedures have been developed. The same should be true for the SLAM analysis of production components containing solid inclusions.

REFERENCES

1. D. E. Yuhas, T. E. McGraw, and L. W. Kessler, Differentiation of Various Flaw Types in Ceramics Using the Scanning Laser Acoustic Microscope, Proc. ARPA/AFML Conf. on Quantitative NDE. LaJolla, CA. 1979.

2. B. T. KHURI-YAKUB. Nondestructive Evaluation of Structural Ceramic Component Proc. 1979 Ultrasonics Symposium New Orleans Sept. 1979.

3. G. S. Kino, Nondestructive Evaluation, Science Vol. 206, pp 173-180, Oct. 1979.

4. D. E. Yuhas, T. E. McGraw, and L. W. Kessler, Non-Destructive Evaluation of Stainless Steel Bellows and POCO Graphite by Means of Scanning Laser Acoustic Microscope (SLAM). Sandia Report #79-7047, Oct. 1979.

5. D. S. Kupperman, C. Sciammarella, N.P. Lapinsk: A. Sather, D. Yuhas, L. Kessler, and N.F. Fiore, "Preliminary Evaluation of Several NDE Techniques for Silicon Nitride Gas-Turbine Rotors," Argonne National Laboratory Report ANL-77-89, January 1978.

6. D. S. Kupperman, L. Pahis, D. Yuhas, and T. McGraw, Acoustic Microscopy for Structural Ceramics submitted Journal of American Ceramic Society 1979.

7. D. E. Yuhas, and L. W. Kessler, Scanning Laser Acoustic Microscope Applied to Failure Analysis, Proc. ATFA - 78 IEEE Inc., New York, N. Y. Catalog No. 78CHI407-6 REG6., pp. 25-29 (1978).

8. Private communication: Fred Lange, Rockwell Science Center, Thousand Oaks, CA.